Wavefront Healing and Tomographic Resolution of Mantle Plumes

Jing Xue

Thesis submitted to the Faculty of the

Virginia Polytechnic Institute and State University

in partial fulfillment of the requirements for the degree of

Master of Science

in

Geosciences

Ying Zhou, Chair

John A. Hole

Scott D. King

August 7, 2014

Blacksburg, Virginia

Keywords: Seismic tomography; Computational seismology; Theoretical seismology;

Wave scattering and diffraction; Wave propagation.

Wavefront Healing and Tomographic Resolution of Mantle Plumes

Jing Xue

(ABSTRACT)

To investigate seismic resolution of deep mantle plumes as well as the robustness of the anti-correlation between bulk sound speed and *S* wave speed imaged in the lowermost mantle, we use a Spectral Element Method (SEM) to simulate global seismic wave propagation in 3-D wavespeed models and measure frequency-dependent *P*-, *S*-, *Pdiff*- and *Sdiff*- wave traveltime anomalies caused by plume structures in the lowermost mantle. We compare SEM time delay measurements with calculations based on ray theory and show that an anti-correlation between bulk sound speed and *S*-wave speed could be produced as an artifact. This is caused by different wavefront healing effects between *P* waves and *S* waves in thermal plume models. The bulk sound speed structure remains poorly resolved when *P*-wave and *S*-wave measurements are at different periods with similar wavelength. The differences in wave diffraction between the two types of waves depend on epicentral distance and wave frequency. The artifact in anti-correlation is also confirmed in tomographic inversions based on ray theory using *Pdiff* and *Sdiff* time delay measurements made on the SEM synthetics. This indicates a chemical origin of "superplumes" in the lowermost mantle may not be necessary to explain observed seismic traveltimes. The same set of *Pdiff* and *Sdiff* measurements are inverted using finite-frequency tomography based on Born sensitivity kernels. We show that wavefront healing effects can be accounted for in finite-frequency tomography to recover the true velocity model.

Acknowledgments

I would like to express the deepest appreciation to my advisor, Prof. Ying Zhou for the continuous support of my study and research. She is a great advisor guiding me to theoretical and computational seismology. Her patience and guidance helped me in all the time of research and writing this thesis.

I also wish to thank my committee, Prof. John A. Hole and Prof. Scott D. King for their insightful comments, hard questions and encouragement. Prof. Hole has provided constructive suggestions to my research, and discussions with him during committee meetings help me improve my research in many ways. Prof. King has been a great help on mantle plumes. His immense knowledge inspired my interests on Geodynamics.

My sincere thanks also goes to administrative staff, Connie Lowe, Ellen Mathena, Mary McMurray, Jo Thomason and Sharon Collins for their kind assistance, and Jim Langridge, Mark Lemon and James Dunson for their technical support in the past two years. My special thanks to Llyn Sharp for her thoughtful help when I worked at the Museum as a GTA.

I would like to thank the Advanced Research Computing (ARC) at Virginia Tech for providing

computational resources and especially Justin Krometis at ARC for technical support.

I thank my fellow students, Youyi Ruan, Kui Liu, Kai Wang, Pavithra Sekhar, Aida Farough, Shreya Singh, Didem Beskardes, Kathy Davenport, Anna Hardy, Lindsay Sabey, Kannikha Kolandaivelu for their encourage and help and all the fun we have. I will miss the good time with my Chinese friends Qimin Wu, Liang Han, Meijing Zhang, Wei Cheng and Hui Tang.

I would like to thank my parents and parents-in-law for their continuous support. At last, I want to thank my husband, Kai Deng for his accompany and support.

Contents

List of Figures

Chapter 1

Introduction

The lowermost 200 to 300 km of the Earth's mantle, referred to as D" layer, plays an important role in mantle convection and core-mantle interaction. If heat flux from the core is sufficiently high, the thermal boundary layer would become unstable and produce buoyant upwellings. The upwellings, or mantle plumes, are often related to heat flux and topography anomalies at the surface. The existence of deep mantle plumes under a number of hot spots have been confirmed in global finite-frequency tomographic studies (e.g., Montelli et al., 2006; Nolet et al., 2006).

Seismic tomography based on ray theory have also revealed two large wavespeed anomalies, known as "superpluemes", at the bottom of mantle, one under Africa and the other under the southern Pacific (Robertson & Woodhouse, 1995; Masters et al., 2000; Houser et al., 2008). The anomalies are characterized by large reductions in S-wave speed and have a much broader lateral extent than a hot upwelling plume. The exact location of the "superplumes" shows significant

variations among tomographic models (Su & Dziewonski, 1997; Masters et al., 2000; Ishii & Tromp, 2004; Trampert et al., 2004; Houser et al., 2008; Manners, 2008).

It is known that the direct seismic observables are *P*- and *S*-wave speed anomalies, bulk sound speed, which depends on the bulk modulus, have been calculated from *P* wave and *S* wave speeds. The "superplumes" are strong S-wave anomalies but much weaker P-wave anomalies, resulting an "anti-correlation" between bulk sound speed and S-wave speed anomalies in those regions. Karato & Karki (2001) pointed out that the ratio between *S*- and *P*-wave perturbations $R_{s/p} = \delta \ln v_s / \delta \ln v_p$ in the lowermost mantle exceeds the threshold for pure thermal anomalies. The anti-correlation between bulk sound and shear wave speed perturbations has been explained as compositional anomalies caused by variations in prevoskite, partial melting or subducted oceanic crust at the base of the mantle (e.g. Deschamps & Trampert, 2003; Thorne & Garnero, 2004; Tan & Gurnis, 2005). Davies et al. (2012) argued that even the inclusion of chemical heterogeneities cannot produce a large-scale lower mantle anti-correlation between bulk sound speed and shear velocity anomalies. They concluded that the seismically observed anti-correlation is more likely caused by phase transition from perovskite to post-perovskite and it occurs only in regions where post-perovskite is stable. Cobden et al. (2012) compared different mantle models in reproducing long-wavelength seismic *Pdiff* and *Sdiff* data statistically and suggested that a model with post-perovskite-bearing CMB regions fit seismic data better than a post-perovskite-free CMB region.

In global tomography, body wave phases including direct *P* and *S*, *PcP*, *ScS*, *Pdiff*, *Sdiff*, *PKP* and *SKS* have been used to determine seismic heterogeneities in the lower mantle (Masters et al., 2000; Kárason & van der Hilst, 2001; Montelli et al., 2006; Ritsema & van Heijst, 2002; Lay,

2007). Kárason & van der Hilst (2001) showed that the inclusion of core diffracted (*Pdiff*) and refracted (*PKP*) phases can significantly improve the resolution in the 300 km of the lowermost mantle. Compared to tomographic results using *P* waves only, the inclusion of *Pdiff* enhances the amplitude and resolution of slow anomaly in the southern Pacific in their P-wave velocity model as the diffracted waves travel along the core-mantle boundary (CMB).

Travel time data used in many lower mantle global tomographic studies are at a period of about 20 seconds (e.g., Masters et al., 2000; Kárason & van der Hilst, 2001). Traveltime anomalies caused by mantle heterogeneities "heal" as waves propagate beyond the heterogeneity, The strength of wavefront healing depends seismic wavelength, epicentral distance as well as earthquake source radiation (e.g., Nolet & Dahlen, 2000; Hung et al., 2001; Zhou et al., 2004; Tromp et al., 2005; Malcolm & Trampert, 2011; Schuberth et al., 2012). Ray theory, which does not account for off-ray structures, fails to explain observed seismograms when anomaly size is comparable to the size of the Fresnel zone. Hwang et al. (2011) analyzed time delays of *SSS* waves between 5 s and 20 s period caused by shear wave velocity structure obtained from geodynamic plume models, and concluded that wavefront healing is strong enough that seismic traveltime anomalies caused by deep mantle plumes may become seismically "invisible". Malcolm & Trampert (2011) discussed the artifacts of anti-correlation caused by wavefront healing in ray-theoretical tomography using time delays of direct *P* and *S* waves. They argued that unaccounted wave diffractional effects can lead to bias in anti-correlation between bulk sound speed and *S*-wave speed perturbations for both fast and slow anomalies in body wave tomography, and composite properties such as bulk sound speed must be interpreted carefully to avoid such bias.

In this study, we focus on wave diffractional effects in core-mantle-boundary diffracted *P* and *S* waves (*Pdiff*, *Sdiff*), which have been proved to provide best coverage in the lowermost mantle. We investigate how wavefront healing affects resolution of seismic anomalies in tomographic models that have been associated with plumes or superplumes. We use the Spectral Element Method (Komatitsch & Tromp, 1999, 2002) to simulate global seismic wave propagation in 3-D thermal plume models and measure frequency-dependent *P*-wave and *S*-wave time delays caused by plume structures in the lowermost mantle.

Core-mantle-boundary diffracted waves, *Pdiff* and *Sdiff*, travel along the core-mantle boundary and only sample seismic anomalies in lowermost mantle in our numerical simulations. To investigate lateral resolution of plume anomalies constrained by *Pdiff* and *Sdiff* waves, anomalies used in this paper extend from the CMB to 400 km above the CMB. It is worth noting that plume structures at shallower depths do not affect core-mantle-boundary diffracted waves in our numerical experiments. Wave speed perturbations in the plume anomalies are -1.5% in *P* wavespeed and -3% in *S* wavespeed at the center of the plume. The ratio $R_{s/p} = \delta \ln v_s / \delta \ln v_p$ in the plume models is 2.0 and perturbations in bulk sound speed and S-wave speed are positively corrected in the synthetic plume models. We investigate how the anomalies are resolved in ray-theoretical tomography and finite-frequency tomography.

We compare measured SEM time delays to calculations based on ray theory, and investigate wavefront healing in *P* waves and *S* waves. We show that an apparent anti-correlation between bulk sound speed and shear velocity anomalies could be produced as an artifact of unaccounted wavefront healing effects in ray-theoretical analysis. The measured SEM traveltimes at different

periods are inverted for *P* wave and *S* wave structures using ray-theoretical tomography. In general, the "smearing" is stronger in *P*-wave models, and the recovered anomalies are weaker in amplitude and larger in size compared to the input model. An "anti-correlation" between bulk sound speed and *S* wave speed as an artifact is seen in all models recovered in ray-theoretical tomography at periods between 12$\sim$20 seconds.

Finally, we calculate finite-frequency sensitivity kernels for core-mantle-boundary diffracted waves (*Pdiff*, *Sdiff*) to account for wave diffraction effects. Calculations based on finite-frequency sensitivities fit the measured traveltimes better than those based on ray theory. Finite-frequency tomography using diffracted P and S waves confirms that the size and strength of mantle plume anomalies in the lowermost mantle can be recovered using Born sensitivity kernels.

Chapter 2

Forward Modeling

We simulate seismic wave propagation in three-dimensional plume models using the Spectral Element Method (Komatitsch & Tromp, 1999, 2002). The plume anomalies in the wavespeed models have a cylindrical geometry in the lowermost mantle. The vertical extent of the plumes is 400 km and the radius varies from 300 km to 1000 km. Wave speed perturbation in the center of the plumes is -1.5% in *P* wavespeed and -3% in *S* wavespeed. The ratio $R_{s/p} = \delta \ln v_s / \delta \ln v_p$ in the synthetic plume models is less than 2.7, which is consistent with a thermal origin in mineral physics models (Karato & Karki, 2001).

2.1 Seismic wave propagation simulation in 3-D Earth models

To reduce numerical noise in SEM simulation at the periods we are interested in, the global mesh in SEM is represented by $640 \times 640 \times 6$ spectral elements on the free surface. The simulations are

accurate down to the period of about 8 seconds in spherically symmetric earth models. The size of the spectral element is about 35 km in the lowermost mantle. All seismograms are calculated for purely elastic models. To avoid vertical wave speed boundaries, both P and S wave velocity perturbations have a Gaussian structure with maximum perturbation at the center of the plume. We simulate seismic wave propagation in 3-D plume models with different anomaly size and compare measured delays to ray-theoretical predictions.

P-wave and *S*-wave time delays caused by the plume anomalies are measured at periods of 12.5 s, 15 s and 20 seconds on vertical component (*P* wave) and transverse component (*S* wave) seismograms, respectively. We investigate how wavefront healing affects time delays caused by thermal mantle plumes by comparing frequency-dependent time delays measured on SEM seismograms and predicted time delays based on ray theory. We calculate the "apparent" bulk sound speed perturbations from measurements over an epicentral distance between 60° and 140° degree, and investigate the correlation between bulk sound speed and *S*-wave speed perturbation across different wave periods.

2.2 Wave diffraction in mantle plume models

In the first simulation, both the earthquake and stations are located at the equator (Fig. 2.1). We record seismograms at stations with epicentral distances ranging from 60° to 140°. The center of the anomaly is located 60° away from the seismic source, and the radius of the plume is 500 km. *Pdiff* as well as some of *P* wave rays travel through the plume anomaly. The center of the plume is

not always located half way between the source and receiver in this source-receiver configuration.

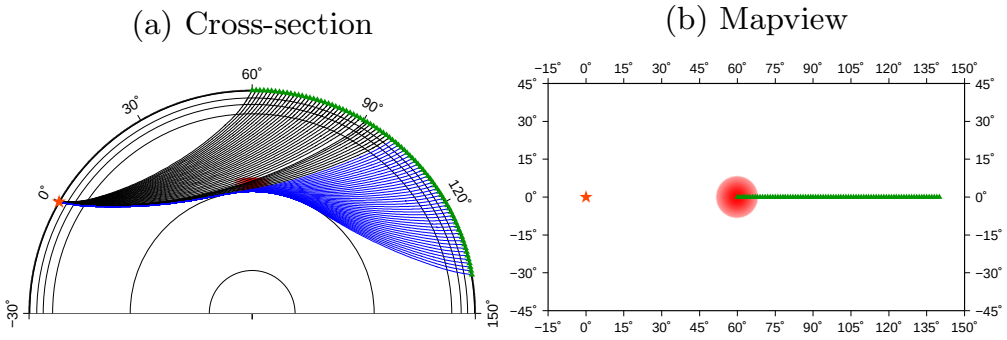

Figure 2.1: Source and receiver geometry in SEM simulations. (a) Cross-section and (b) map view. The orange star shows the location of seismic source, and green triangles are 81 receivers located at epicentral distances from 60° to 140° with 1° spacing. Black and blue lines in (a) are ray paths of *P* and *Pdiff* waves, respectively. The plume anomaly has a radius of 500 km and vertical extent of 400 km.

We measure travel time anomalies of the first *P* and *S* arrivals on the seismograms at different frequencies. The ray-theoretical response a minor-arc body wave to a moment tensor earthquake source can be written as (Dahlen & Tromp, 1998, Chapter 12.5),

$$s(\omega) = A(\omega)e^{-i\omega T}e^{-i\phi_s(\omega)} \tag{2.1}$$

where $s(\omega)$ is the response of the body wave and T is the associated travel time along the ray path. The amplitude $A(\omega)$ accounts for source excitation and geometrical spreading and $\phi_s(\omega)$ is the phase spectra of the source time function.

While the expression of ray-theoretical body-wave response is strictly valid only when ω approaches infinity, transfer functions can be used to quantified differences between synthetic and observed seismograms to estimate frequency-dependent traveltime anomalies, (e.g. Laske & Masters, 1996; Zhou et al., 2006; Kennett & Fichtner, 2012),

$$F(\omega) = \frac{s(\omega)}{s_0(\omega)} = \frac{A(\omega)e^{-i\omega T(\omega)}}{A_0(\omega)e^{-i\omega T_0(\omega)}}. \tag{2.2}$$

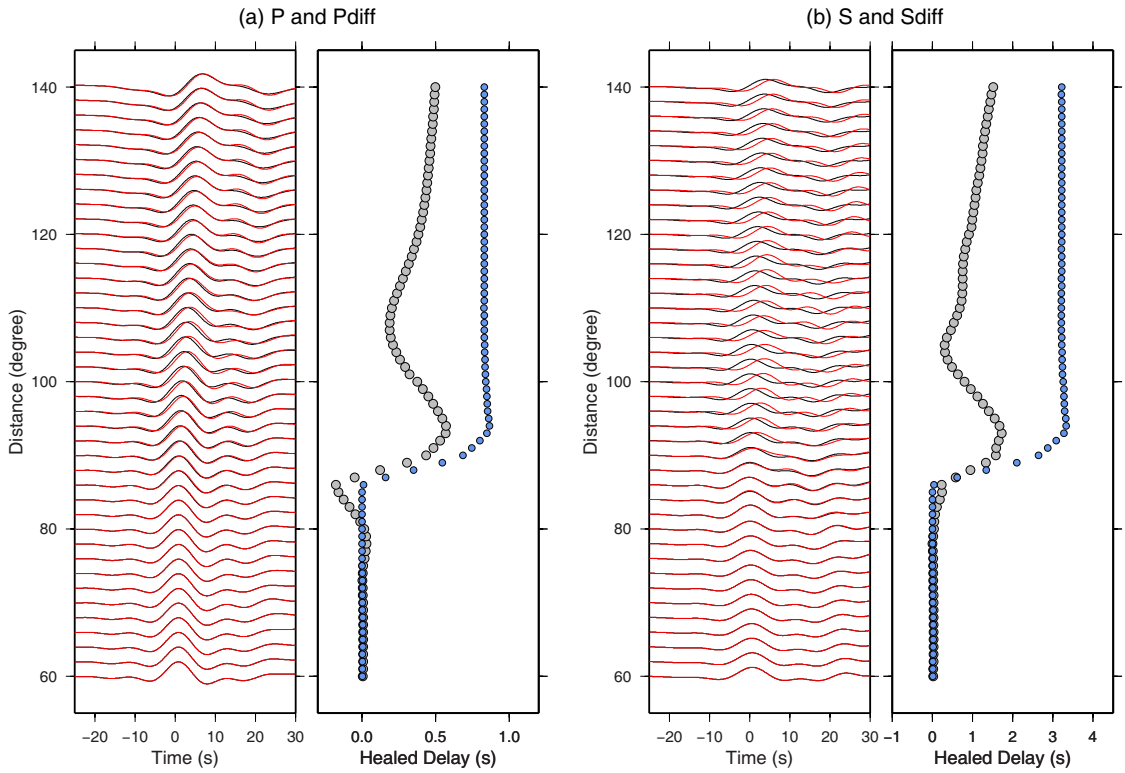

Figure 2.2: (a) Example SEM seismograms of *P* and *Pdiff* waves in the plume model as shown in Fig. 2.1. The radius of the plume anomaly is 500 km. The corresponding ray prediction (blue dots) and "healed" delay time at a period of 20 seconds (grey dots) at each station are shown as a function of epicentral distance. (b) The same as (a) but with *S* and *Sdiff* phases.

Where $F(\omega)$ is the transfer function, $s(\omega)$ is the observed spectra of a tapered body-wave seismogram and $s_0(\omega)$ is the spectra of the tapered synthetic seismogram in the reference model. The traveltime anomalies can be estimated from the logarithm of the transfer function,

$$\delta T = T - T_0 = -\omega^{-1}\mathrm{Im}\{\ln F(\omega)\}. \tag{2.3}$$

Fig. 2.2 shows differences between measurements and ray predictions as a function of epicentral distance. The maximum delay times in ray predictions are 0.83 seconds for *P* waves and 3.21 seconds for *S* waves, and "healed" traveltime is about 0.43 seconds in *P* waves and 1.07 seconds in *S* waves at a distance of 125°. The "dispersion" of measured body wave traveltimes depends on

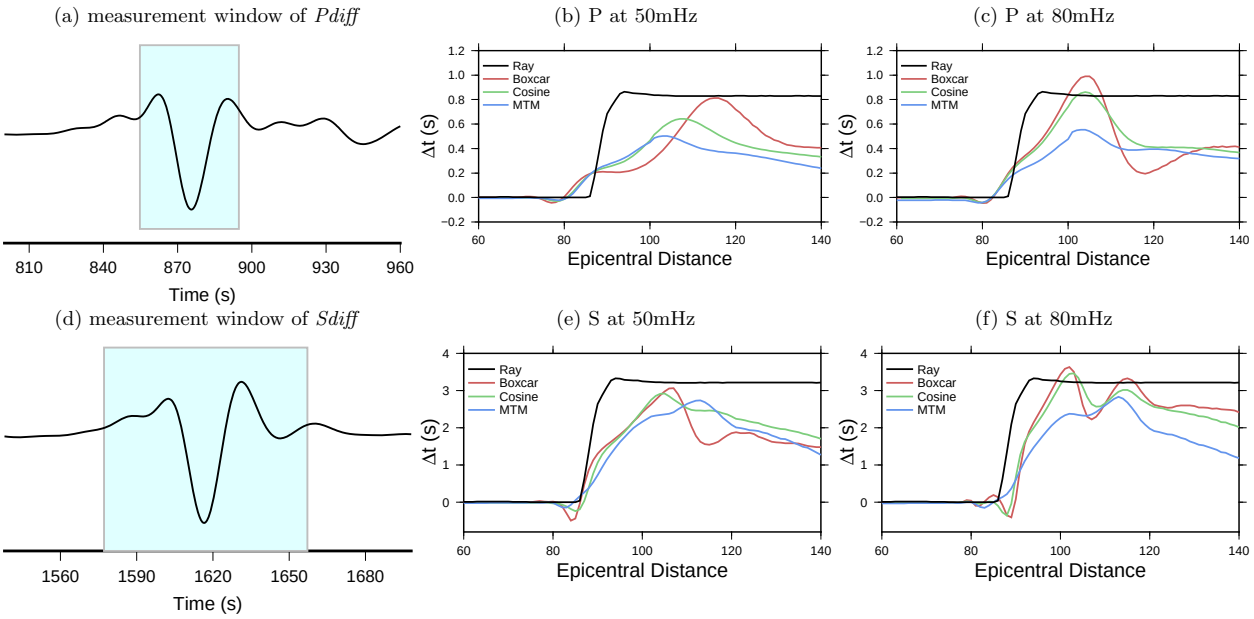

Figure 2.3: Measurement window of (a) *Pdiff* and (d) *Sdiff*. (b) and (c) are *P*-wave time delays at 20 s (50 mHz) and 15 s (67 mHz) using different measuring method. (e) and (f) are the same as (b) and (c) but for *S* waves. The time delays are caused a plume anomaly with radius of 300 km.

frequency averaging. Fig. 2.3 shows a comparison of time delays measured at various frequencies using a time-domain cosine taper, boxcar taper and a Slepian multi-taper with four 1.5π spheroidal eigentapers (Thomson, 1982). Time delays obtained using different measurement techniques differ significantly. The traveltimes discussed in the rest of the paper are made using cosine taper.

In Fig. 2.4, we investigate wavefront healing effects in *P* and *Pdiff* waves as the radius of the plume varies from 300 km to 1000 km. Wavefront healing effect which is expected to be stronger for small heterogeneities becomes significant for plumes with a radius less than 500 km. In the case of the smallest anomaly in our simulation ($R = 300$ km), time delay at 130° measured at 50 mHz is healed by about 71% compared to ray predictions. In the case of a big plume ($R = 1000$ km), healing reduces to 22% at 50 mHz at this epicentral distance. Measurements show apparent

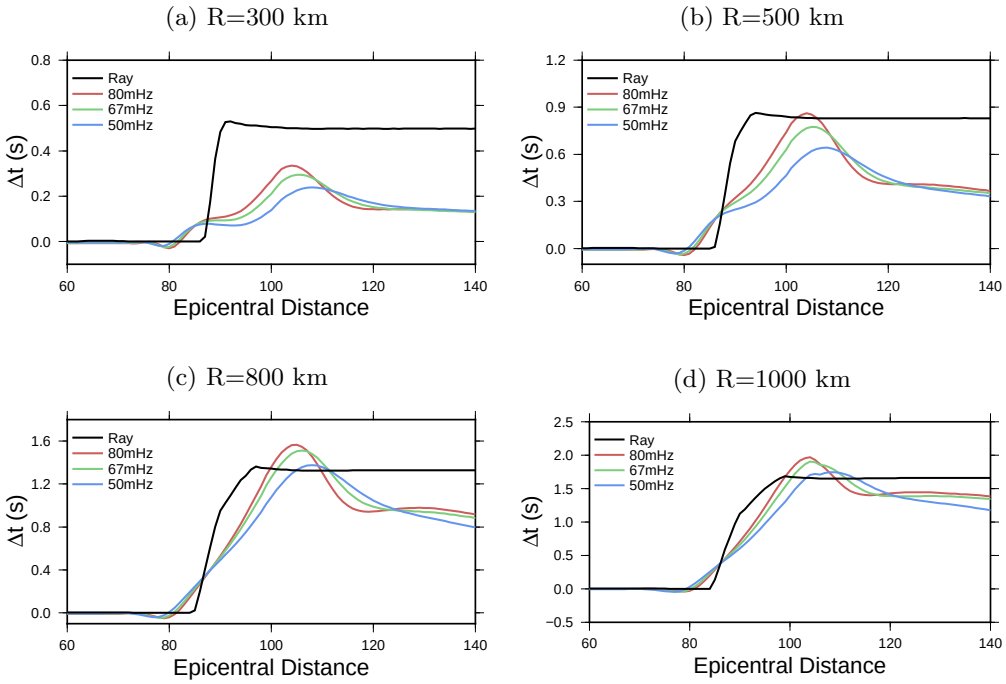

Figure 2.4: Measured time delays at different frequencies and predicted ray-theoretical time delays (black) for plume anomalies with different lateral radius of $R = 300$ km, $R = 500$ km, $R = 800$ km and $R = 1000$ km. Source and receivers are shown in Figure 2.1.

"dispersion" variations with epicentral distance. At epicentral distances larger than $100°$, time delays are healed more at larger distances. The time delays at distances less than $89°$ is zero in ray predictions while the measured delays at distances between $75°$ and $89°$ are not zero due to wave diffraction. At about $100°$ distance, traveltime anomalies increase rapidly with epicentral distances as scattered waves generated by the anomaly interfere constructively with the reference wave, and then decrease as the interference becomes destructive. At a distance of $\sim 115°$, dispersion becomes very weak. In general, time delays at longer periods are smaller, this is understood as stronger healing effects are expected.

2.3 Bulk sound speed

Thermal anomalies in the mantle are associated with increases (or decreases) in both bulk modulus and shear modulus, and therefore the correlation between bulk sound speed and shear wave speed perturbations helps distinguish between thermal or chemical origin of seismic anomalies (Masters et al., 2000; Trampert et al., 2001; Karato & Karki, 2001).

In seismic tomography, direct observables are *P*-wave and *S*-wave traveltimes, which can be used to invert for *P*-wave and *S*-wave speed perturbations. The *P*- and *S*-wave speeds are related to elastic moduli and density by

$$v_p^2 = \frac{K + 4\mu/3}{\rho}, \qquad v_s^2 = \frac{\mu}{\rho}, \tag{2.4}$$

where K is bulk modulus, μ is shear modulus and ρ is density.

Bulk sound speed, which depends only on bulk modulus and density, is an important property of Earth materials. Bulk sound speed can be calculated from *P*- and *S*- wave speeds,

$$v_c^2 = v_p^2 - \frac{4}{3}v_s^2, \tag{2.5}$$

where $v_c^2 = K/\rho$.

In ray theory, a time delay caused by a small perturbation in wavespeed along a ray segment can be written as

$$\delta t = -\left(\frac{\delta v}{v}\right) t, \tag{2.6}$$

where v is the reference wavespeed and t is the theoretical travel time in the ray segment. Wavespeed

perturbations are related to traveltime anomalies by

$$\frac{\delta v_p}{v_p} = \frac{\delta t_p}{t_p}, \qquad \frac{\delta v_s}{v_s} = \frac{\delta t_s}{t_s}, \tag{2.7}$$

where $\delta v_p/v_p$ and $\delta v_s/v_s$ are fractional perturbations in *P*-wave and *S*-wave speeds, and $\delta t_p/t_p$ and $\delta t_s/t_s$ are fractional *P*-wave and *S*-wave traveltime anomalies. The perturbation in bulk sound speed can be written as

$$\begin{aligned}\left(\frac{\delta v_c}{v_c}\right)_{ray} &= \left(\frac{v_p^2}{v_c^2}\right)\left(\frac{\delta v_p}{v_p}\right) - \frac{4}{3}\left(\frac{v_s^2}{v_c^2}\right)\left(\frac{\delta v_s}{v_s}\right) \\ &= \left(\frac{\delta v_s}{v_s}\right)\left(\frac{v_s^2}{v_c^2}\right)\left(\frac{1}{R_{s/p}}\frac{v_p^2}{v_s^2} - \frac{4}{3}\right).\end{aligned} \tag{2.8}$$

This implies when $R_{s/p} \leq 2.7$, the perturbation in bulk sound speed should be positively correlated to that in *S* wave speed assuming an average $v_p = 13.6$ km/s and $v_s = 7.2$ km/s in the lowermost mantle.

Finite-frequency effects can be significant when the length scale of a wavespeed anomaly is comparable to the size of the Fresnel zone. In this case, observed time delays will be different from ray-theoretical predictions due to wave diffraction. We introduce two factors h_p and h_s to quantify wavefront healing in *P* and *S* waves:

$$h_p = \frac{(\delta t_p/t_p)_{obs}}{(\delta t_p/t_p)_{ray}}, \qquad h_s = \frac{(\delta t_s/t_s)_{obs}}{(\delta t_s/t_s)_{ray}}, \tag{2.9}$$

where $(\delta t_p/t_p)_{obs}$ and $(\delta t_s/t_s)_{obs}$ are observed fractional delay times and $(\delta t_p/t_p)_{ray}$ and $(\delta t_s/t_s)_{ray}$ are ray-theoretical predictions. The "apparent" *P* and *S* wavespeed heterogeneities are simply

$$\begin{aligned}\left(\frac{\delta v_p}{v_p}\right)_{apparent} &= \left(\frac{\delta t_p}{t_p}\right)_{obs} = h_p\left(\frac{\delta t_p}{t_p}\right)_{ray} \\ \left(\frac{\delta v_s}{v_s}\right)_{apparent} &= \left(\frac{\delta t_s}{t_s}\right)_{obs} = h_s\left(\frac{\delta t_s}{t_s}\right)_{ray}.\end{aligned} \tag{2.10}$$

The "apparent" bulk sound speed can be calculated from observed travel times,

$$\left(\frac{\delta v_c}{v_c}\right)_{apparent} = \left(\frac{v_p^2}{v_c^2}\right)\left(\frac{\delta v_p}{v_p}\right)_{apparent} - \frac{4}{3}\left(\frac{v_s^2}{v_c^2}\right)\left(\frac{\delta v_s}{v_s}\right)_{apparent}. \tag{2.11}$$

The ratio between apparent and ray-theoretical bulk sound speed perturbations,

$$r = \frac{(\delta v_c/v_c)_{apparent}}{(\delta v_c/v_c)_{ray}} \tag{2.12}$$

can be used to investigate wavefront healing effects in bulk sound speed. Plume models in our simulations are associated with negative bulk sound perturbations. i.e., $(\delta v_c/v_c) < 0$, a negative value of r will indicate an increase in apparent bulk sound perturbation, i.e., $(\delta v_c/v_c)_{apparent} > 0$.

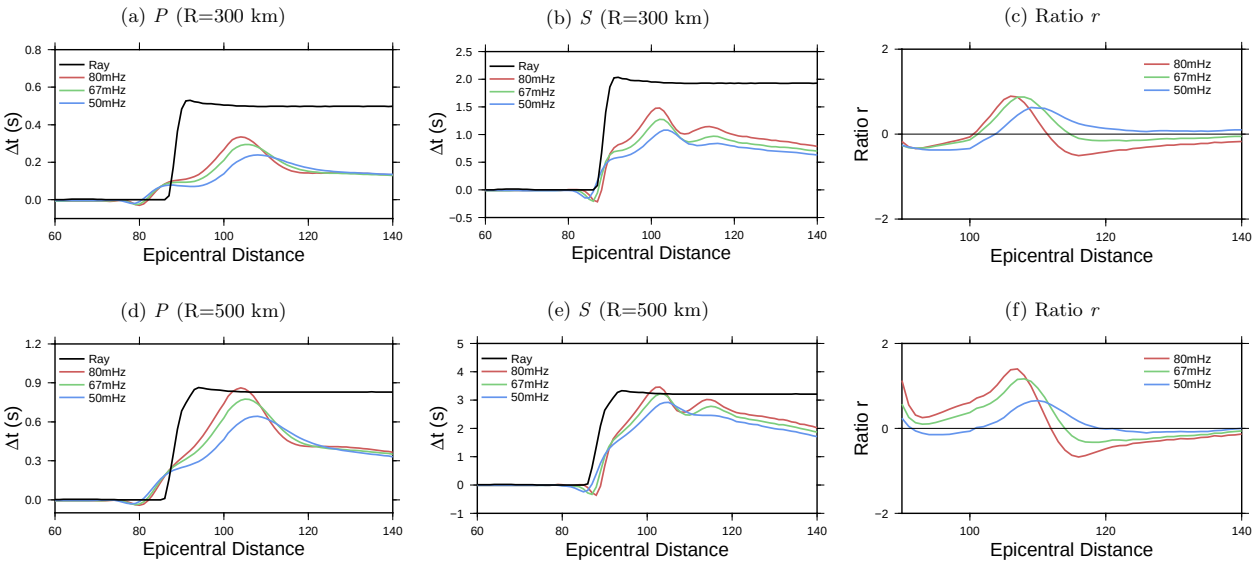

Figure 2.5: Comparison of different healing strength for *P* waves and *S* waves and the bulk sound speed ratio r in Equation (2.12). A negative value of r indicates an artifact of anti-correlation between bulk sound speed and *S*-wave speed perturbations due to different healing rate for *P* waves and *S* waves.

In our simulation, the ratio between *P* wave and *S* wave perturbations in plume is $R_{s/p}$ =2.0, which is consistent with thermal anomalies. We calculate the ratio between the apparent bulk

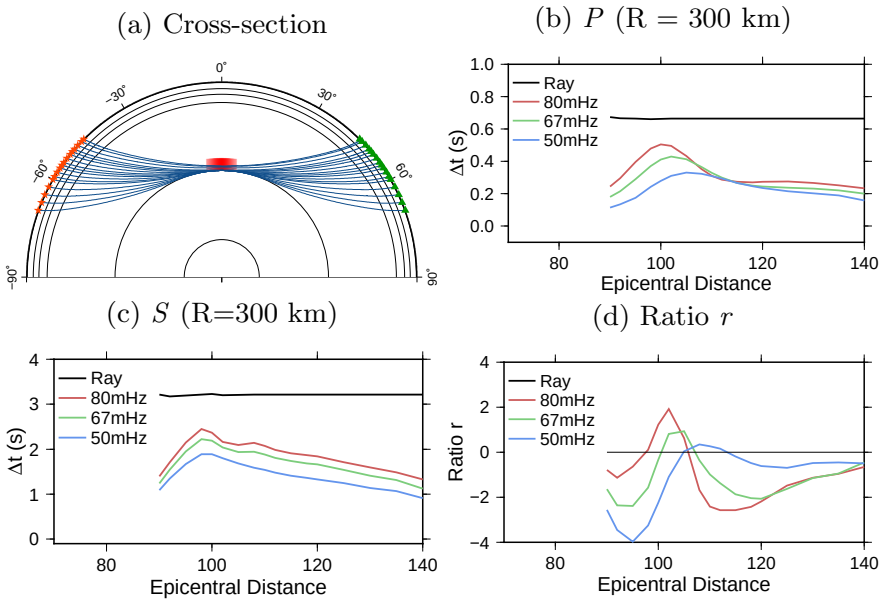

Figure 2.6: (a) Source and receiver geometry in SEM simulation. The plume anomaly is located half way between the source and receiver. (b) Measured time delays and ray theory predicted delays at different frequencies for *P* waves. (c) The same as (b) but for *S* waves. (d) Bulk sound speed ratio r calculated from delays of *P* waves and *S* waves. A negative value of r indicates an artifact of anti-correlation between bulk sound speed and *S*-wave speed perturbations.

sound speed perturbations and ray-theoretical estimates in Fig.2.5. The "apparent" bulk sound speed perturbations are obtained based on SEM measurements.The radii of the plumes in Fig. 2.5 are 300 km and 500 km, and corresponding *P*-wave and *S*-wave measurements are plotted for reference. In general, wavefront healing in *P* waves is stronger than that in *S* waves. A negative ratio r which indicates an anti-correlation between S-wave speed and bulk sound speed anomaly is seen at all periods between 12.5 s to 20 s. The competing destructive and constructive wave interference as discussed in Chapter 2.2 breaks the region of negative ratio r into two distance ranges at about $105°$, except for the 67 mhz and 80 mHz measurements in the case of a large plume ($R = 500$ km) where negative values of r are only seen in diffracted waves at large epicentral distances.

To better understand wavefront healing effects at different epicentral distance, we simulate

wave propagation in a plume model where the plume is located half way between the source and receiver. Both diffracted *P* waves and *S* waves experience stronger healing at larger epicentral distances. The ratio r as a function of distance calculated for this source-receiver geometry in general agrees with Fig. 2.5.

Chapter 3

Ray-theoretical Tomography

We investigate resolution limits of ray theory in tomographic inversions of traveltime anomalies measured on SEM synthetics. Ray theoretical tomography is based on infinite-frequency approximation in which an observed traveltime anomaly δt can be expressed as a one-dimensional linear integral over the ray path:

$$\delta t = -\int_{ray} \left(\frac{\delta v}{v}\right) \frac{dl}{v}. \tag{3.1}$$

where v is the wavespeed in the reference model and $(\delta v/v)$ is fractional wavespeed perturbation along the ray path in the reference model.

The linear inverse problem can be written as

$$\mathbf{Gm} = \mathbf{d}, \tag{3.2}$$

where $\mathbf{G}$ is the kernel matrix, $\mathbf{m}$ is the vector of unknown wavespeed perturbations, and $\mathbf{d}$ is traveltime data vector. Tomographic problems are often ill-posed and regularization such as smoothing

and damping can be applied to obtain an "optimal" solution. To regularize the inverse problem, we apply smoothing to a least-squares inverse problem, and the tomographic problem becomes

$$\|\mathbf{Gm} - \mathbf{d}\|^2 + \lambda\|\mathbf{Sm}\|^2 = minimum. \tag{3.3}$$

where λ is the trade-off parameter.

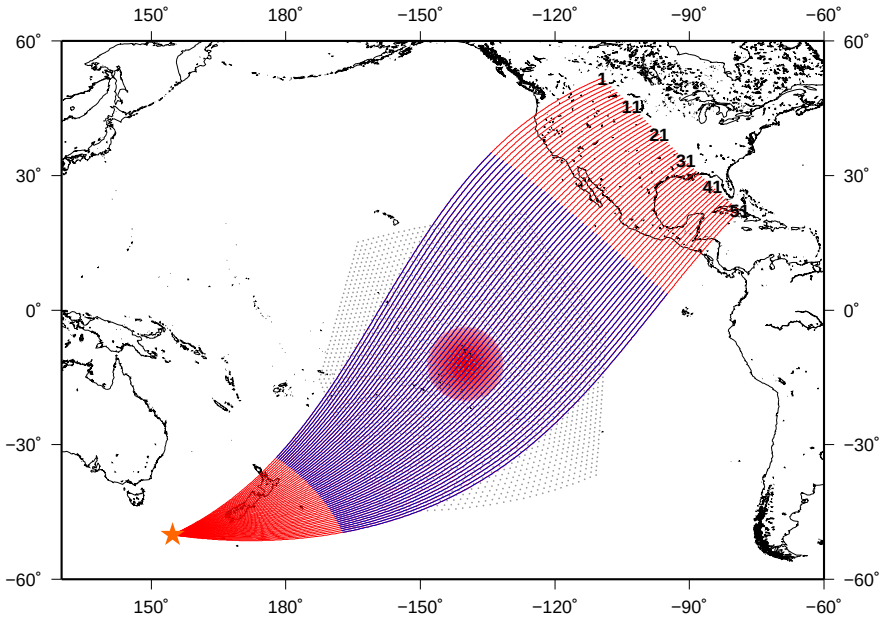

Figure 3.1: Grid points used in inversion and ray path coverage. Black dots show the 3169 grid points on the core mantle boundary. Another set of 3169 grid points are located 400 km above the CMB. The star indicates location of the seismic source and the 51 receivers have the same epicentral distance of 130°. Blue lines show ray coverage at 400 km above the CMB.

In tomographic practice, uncertainties in source parameters and measurements introduce "noise" in data. In our inversion, we add 10% of Gaussian noise to data and the "optimal" model on the trade-off curve can be found by calculating the data misfit function χ^2

$$\chi^2 = \sum_{i=1}^{N} \left(\frac{\sum_{j=1}^{M} G_{ij} m_j - d_i}{\sigma_i} \right)^2 \tag{3.4}$$

where N is the number of time delay measurements, M is the number of unknowns, and σ_i is the

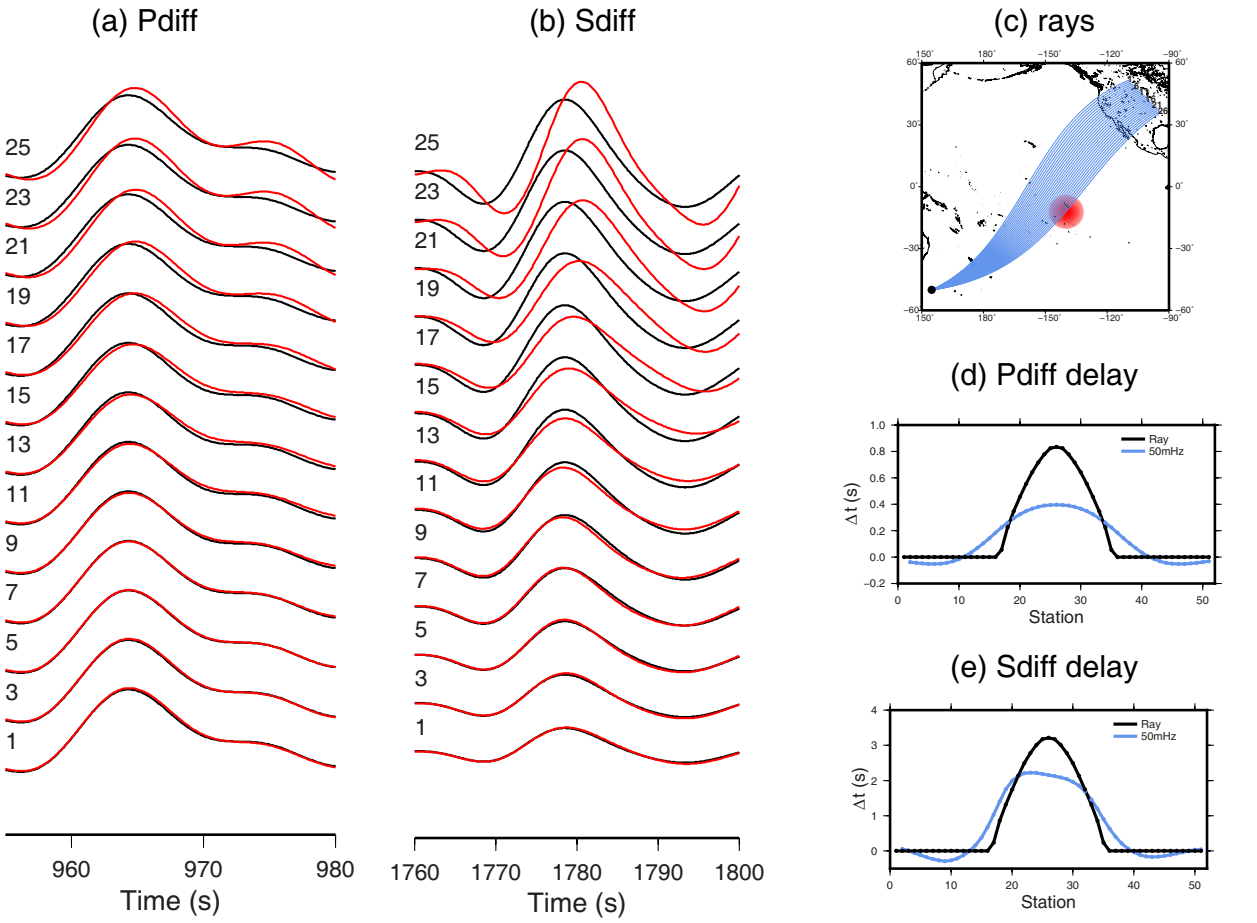

Figure 3.2: Seismograms of (a) *Pdiff* and (b) *Sdiff* at stations number 1 to 25. The radius of the plume anomaly is 500 km. PREM seismograms are plotted in black for reference. (c) Ray paths and location of the plume. (d) and (e) are measured delay time (blue) and ray-theoretical predictions(black).

standard deviation of the Gaussian noise. If noise follows a Gaussian distribution, the data misfit χ^2 should approach the number of data N when the "optimal" model is recovered.

The wavespeed model is parameterized into $3169 \times 2 = 6338$ grid points (Fig. 3.1). The lateral spacing between neighboring grid points is about 60 km at the CMB. We assume seismic velocities can be calculated based on values at six neighboring grid points.

In this study, data used for inversion are time delays caused by 3-D seismic plumes with a lateral

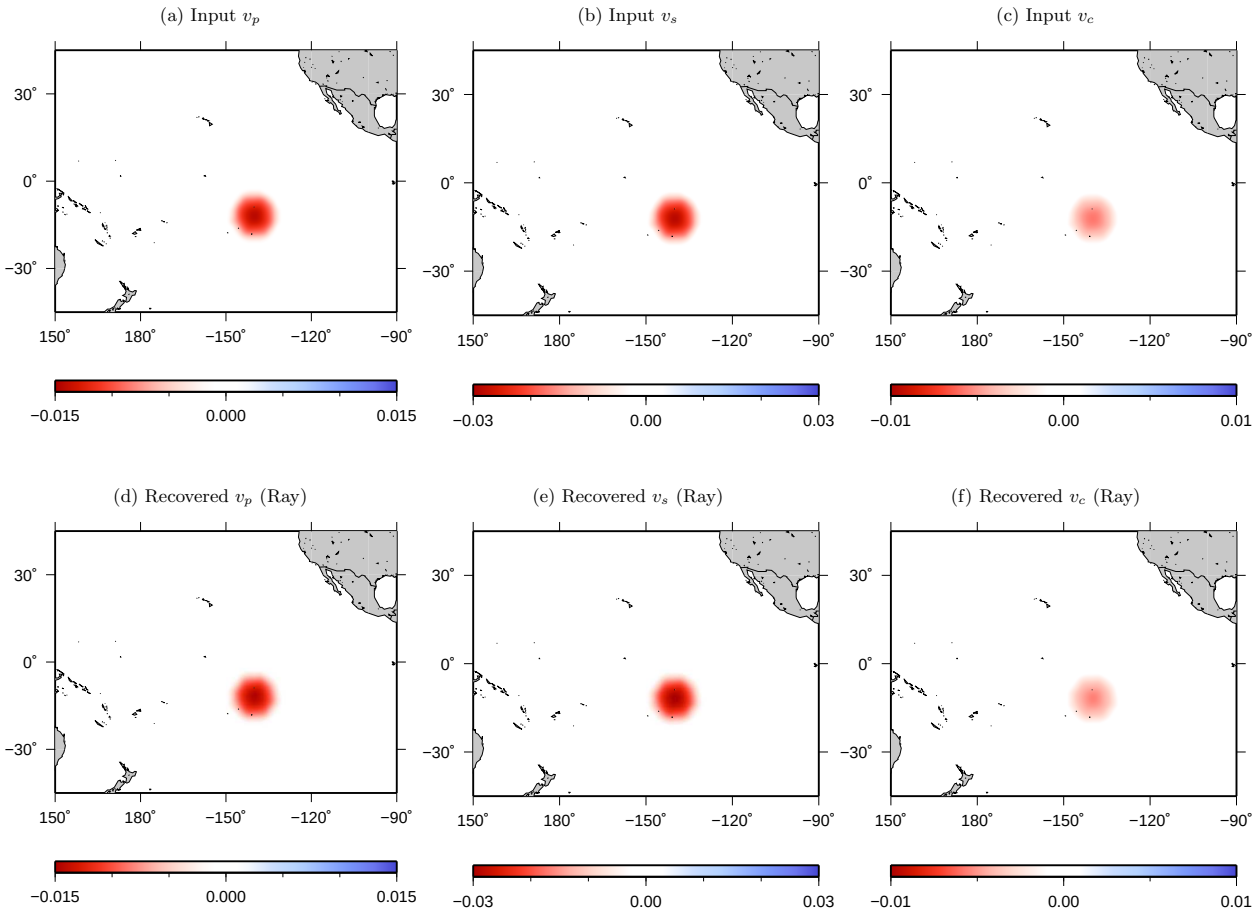

Figure 3.3: Ray theoretical tomography using ray-theory predicted traveltimes. The input P-wave and *S*-wave anomalies are 500 km in radius and have a peak perturbation of -1.5% in *P* wavespeed and -3% in *S* wavespeed. Bulk sound speed anomalies are calculated from *P*-wave and *S*-wave models. The recovered models confirm that ray coverage used in the inversion is sufficient to resolve the plume structure.

radius of 500 km and 1000 km measured from SEM simulated seismograms. Fig. 3.1 shows ray path coverage between a single source and a set of 51 receivers with an epicentral distance of $130\,^{\circ}$.

By rotating the source and receivers, we cover the central Pacific with 9180 *Pdiff* (and *Sdiff*) ray paths. We invert perturbations in *P*-wave and *S*-wave structure separately. The SEM simulation reveals strong wave diffraction effects which are illustrated in (Fig. 3.2). While waves traveling through the center of the plume show time delays and amplification, waves with ray paths away

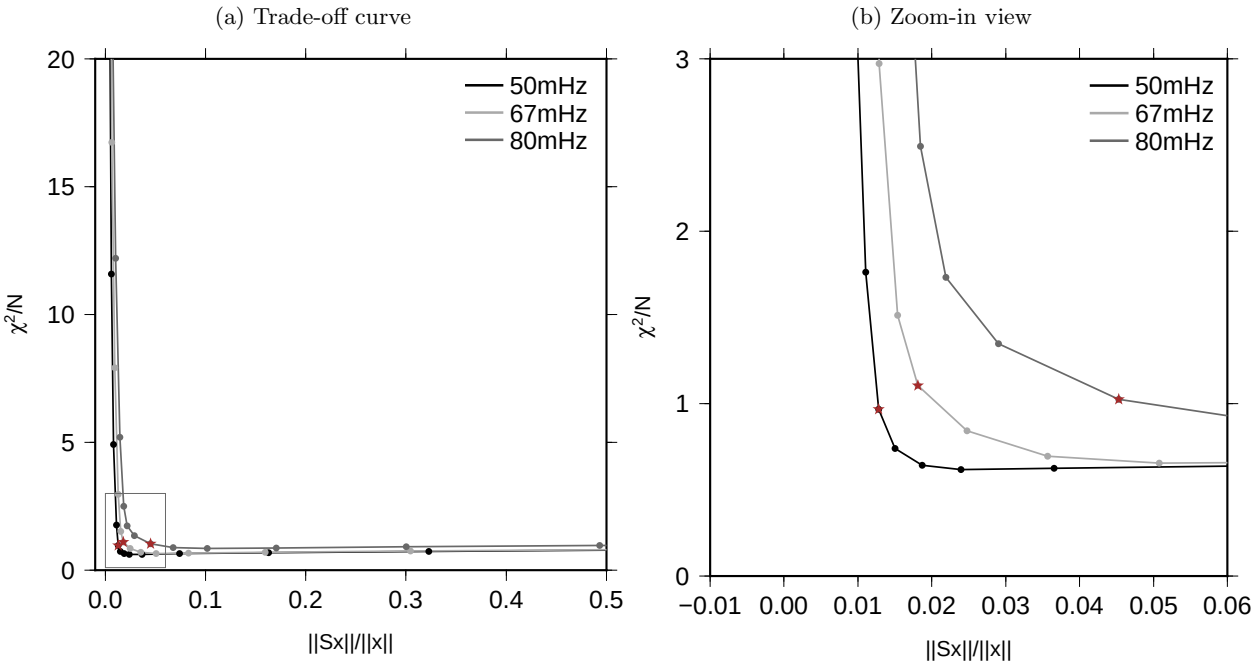

Figure 3.4: Trade-off between data misfit χ^2/N and model roughness $||\mathbf{Sm}||/||\mathbf{m}||$ in ray-theoretical tomography at frequencies of 12.5 s (80 mHz), 15 s (67 mHz) and 20 s (50 mHz). The optimal models are chosen at $\chi^2/N \simeq 1$.

from the plume "feel" the plume and show advances or delays in arrival, depending on geometry.

Before inversion using "ground-truth" SEM measurements, we invert the structure using ray-theory predicted traveltimes. Fig. 3.3 shows that both the size and amplitude of the plume can be well resolved. This confirms that path coverage used in the inversion is sufficient to resolve plume structure.

3.1 Limitations of Ray-theoretical Tomography

We invert the "ground-truth" SEM traveltimes using ray theory tomography, and the trade-off curves between model roughness and data misfit are shown in Fig. 3.4 for data measured at 12.5

s, 15 s and 20 s. The optimal tomographic models are all chosen at $\chi^2/N \simeq 1$. To illustrate limitations of ray theory in seismic tomography, we compare recovered models inverted using data at different frequencies. In Fig. 3.5, the *P* and *S* wavespeed anomalies recovered in ray-theory

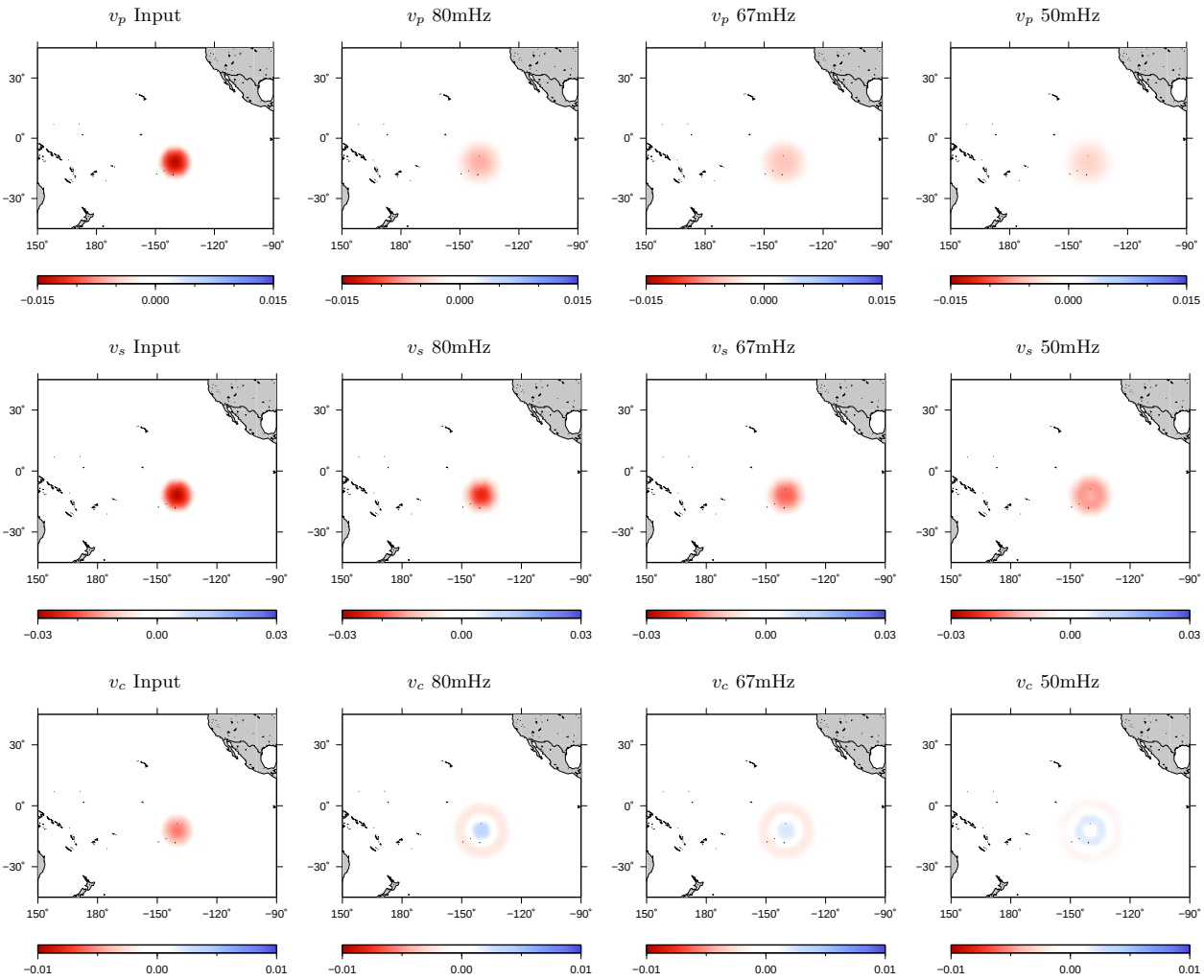

Figure 3.5: Ray theoretical tomography of *P* waves, *S* waves at a period of 12.5 s (80 mHz), 15 s (67 mHz) and 20 s (50 mHz). The recovered *P*-wave, *S*-wave as well as bulk sound speed anomalies are plotted. The input plume anomaly has a radius of 500 km.

tomography are both underestimated in amplitudes. The size and amplitude of anomalies are better recovered with data at shorter periods. For *P* waves and *S* waves of the same period, the size and

anomaly amplitude of the plume is better constrained in *S*-wave tomography. This is expected because the size of the Fresnel zone is smaller for *S* waves than for *P* waves.

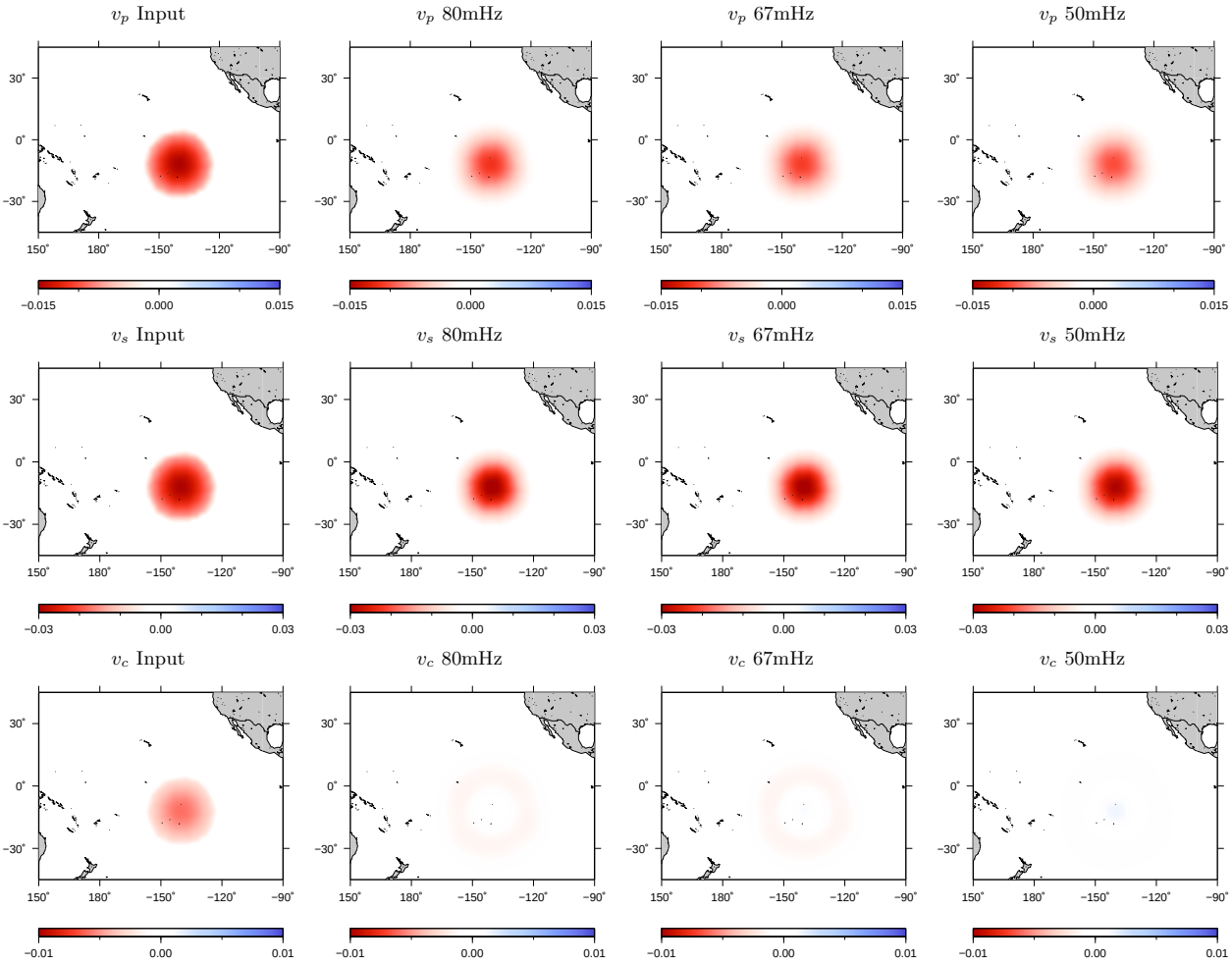

Figure 3.6: Ray theoretical tomography of *P* waves, *S* waves at a period of 12.5 s (80 mHz), 15 s (67 mHz) and 20 s (50 mHz). The recovered *P*-wave, *S*-wave as well as bulk sound speed anomalies are plotted. The input plume anomaly has a radius of 1000 km.

Bulk sound speed heterogeneities may be calculated from *P* and *S* wavespeed heterogeneities (Masters et al., 2000) or jointly inverted with *S* wavespeed heterogeneities using *P*-wave and *S* wave traveltimes (Su & Dziewonski, 1997; Houser et al., 2008; Manners, 2008). In synthetic

experiments, as the inverse problem is over-determined and the recovered model should fit the data equally well (Fig. 3.3). In Fig. 3.5, the recovered bulk sound speed perturbation shows a polarity difference from the input model – the slow anomaly in the input model was recovered as a fast anomaly at the center of the plume. This is the case in all models inverted using data at different periods. The recovered bulk sound anomaly also becomes larger in size.

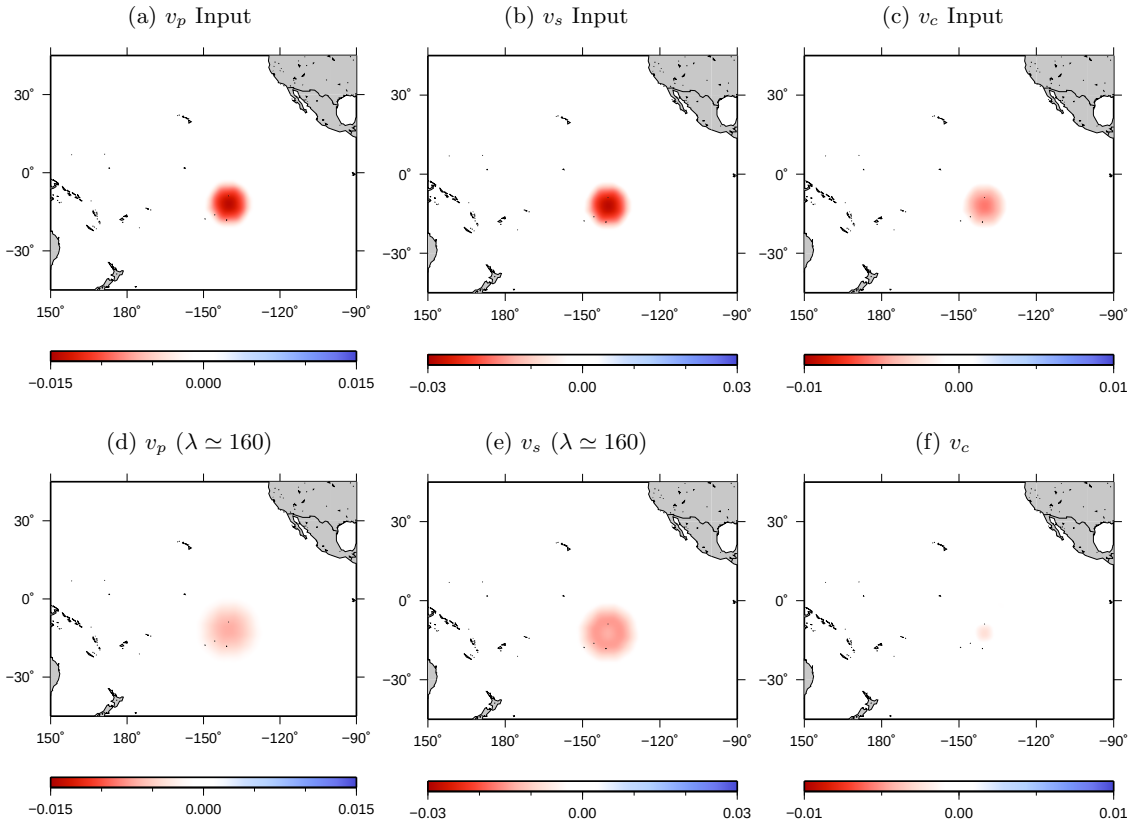

Figure 3.7: Ray theoretical tomography of *P* waves and *S* waves at different frequencies, but a similar wavelength of 160 km. The derived bulk sound speed model shows a negative anomaly at the center of the plume anomaly.

In Fig. 3.6, we show inversions using data generated for a larger plume with a radius of 1000 km. While *P*- and *S* perturbations are reasonably well recovered, their amplitudes are general weaker in recovered models due to wavefront healing, and the "healing" effects are stronger in *P* waves. The derived bulk sound speed structure becomes very weak and also show a positive

polarity at the center of plume at 50 mHz. This is counter intuitive as both *P* and *S* wave structures have been "reasonably" recovered. Amplitude differences in recovered *P*-wave and *S*-wave anomalies due to wave diffraction result in artifacts in "anti-correlation" between bulk sound speed and *S*-wave speed. The effects of wavefront healing should be considered when comparing bulk sound speed and *S* wave heterogeneities recovered using long period data (> 12 s).

It is expected that *P* waves experience stronger wavefront healing compared to *S* waves due to their longer wavelength. In Fig. 3.7 we calculate bulk sound speed anomalies using *P*-wave speeds recovered at a period of 12 seconds and *S*-wave speeds at a period of 20 seconds. At these frequencies, *Pdiff* and *Sdiff* waves have a similar wavelength of about 160 km in the lower mantle. The recovered bulk sound wave speed model is significantly different from the input model. Wave diffraction for *P* waves and *S* waves are intrinsically different as the *P*-to-*P* scattering and *S*-to-*S* scattering have different "radiation" patterns (Nolet & Dahlen, 2000). Therefore, tomography using *P*-waves and *S* waves with the same wavelength do not solve the problem of artifacts in derived bulk sound speed structure.

Chapter 4

Finite-frequency Sensitivity of Diffracted Waves

In finite-frequency theory, seismic observables are sensitive to structures off the ray path and a body wave traveltime at an angular frequency ω can be written as a 3-D volumetric integration over the entire earth Dahlen et al. (2000),

$$\delta T(\omega) = \iiint_{\oplus} \left[K_{\alpha}(\mathbf{x}, \omega) \frac{\delta\alpha}{\alpha} + K_{\beta}(\mathbf{x}, \omega) \frac{\delta\beta}{\beta} \right] d\mathbf{x}^3, \tag{4.1}$$

where $\delta\alpha/\alpha$ and $\delta\beta/\beta$ are fractional perturbations in P- and S- wave speeds, and $K_{\alpha}(\mathbf{x}, \omega)$ and $K_{\beta}(\mathbf{x}, \omega)$ are sensitivity of traveltimes to P and S wavespeed perturbations.

We calculate 3-D sensitivity kernels for time delays between synthetic and observed seismograms based on surface wave mode summation (Zhou, 2009). Examples of traveltime sensitivity to perturbations in compressional wavespeed are shown in Fig. 4.1 and Fig. 4.2, and the sensitivity

of *Sdiff* waves are shown in Fig. 4.3 and 4.4. The sensitivity kernels are calculated for a 50 mHz cosine taper measurement of *Pdiff* and *Sdiff* delays at the distance of 130°. The *Pdiff* sensitivity kernels show a very wide Fresnel zone in the lowermost mantle comparing to the size of plume. The cross-sections show strongest sensitivities about 200 km above the CMB in *Pdiff* kernels and about 100 km above the CMB in *Sdiff* kernels and a "doughnut hole" structure in the plane perpendicular to the ray path is seen in both P and S wave kernels. Fig. 4.2 and 4.4 show mapviews of sensitivity kernels of *Pdiff* and *Sdiff* at the CMB as well as $\sim$300 km above CMB. The plume samples different parts of the *P* and *Sdiff* waves sensitivity at different stations. The *Sdiff* sensitivities in most stations are not symmetric with respect to the reference ray due to radiation of the strike slip source (Fig. 4.4).

An advantage of finite-frequency theory is that the effect of source radiation, windowing and tapering in data measurement can be taken into account in the calculation of finite-frequency sensitivity kernels. Fig. 4.5 shows predicted time delays caused by the plume at different stations using finite-frequency sensitivity kernel for cosine measurements fit data very well while ray-theoretical calculations overestimated delay times almost by a factor of two. S-wave measurements are less well fit due to limited resolution in wave propagation simulations. In Fig. 4.5, we show that when there is no wavespeed perturbations in the element (37.5 km) just above the core-mantle-boundary, the fit between measurements and kernel predictions becomes much better. Improving the accuracy of SEM simulations on core-mantle diffracted S waves is beyond the scope of this study.

Following the same inversion scheme as described in Chapter 3, we inverted SEM measurements at 20 seconds period using Finite-frequency sensitivity kernels, and choose the "optimal"

model at $\chi^2/N \simeq 1$. The inverted *P*-wave speed model from ray theoretical tomography and finite-frequency tomography using the same measurements at 50 mHz are shown in Fig. 4.6 . The input model is well recovered in finite-frequency tomography. This is not surprising as predictions based on Finite-frequency sensitivity agree well with measurements.

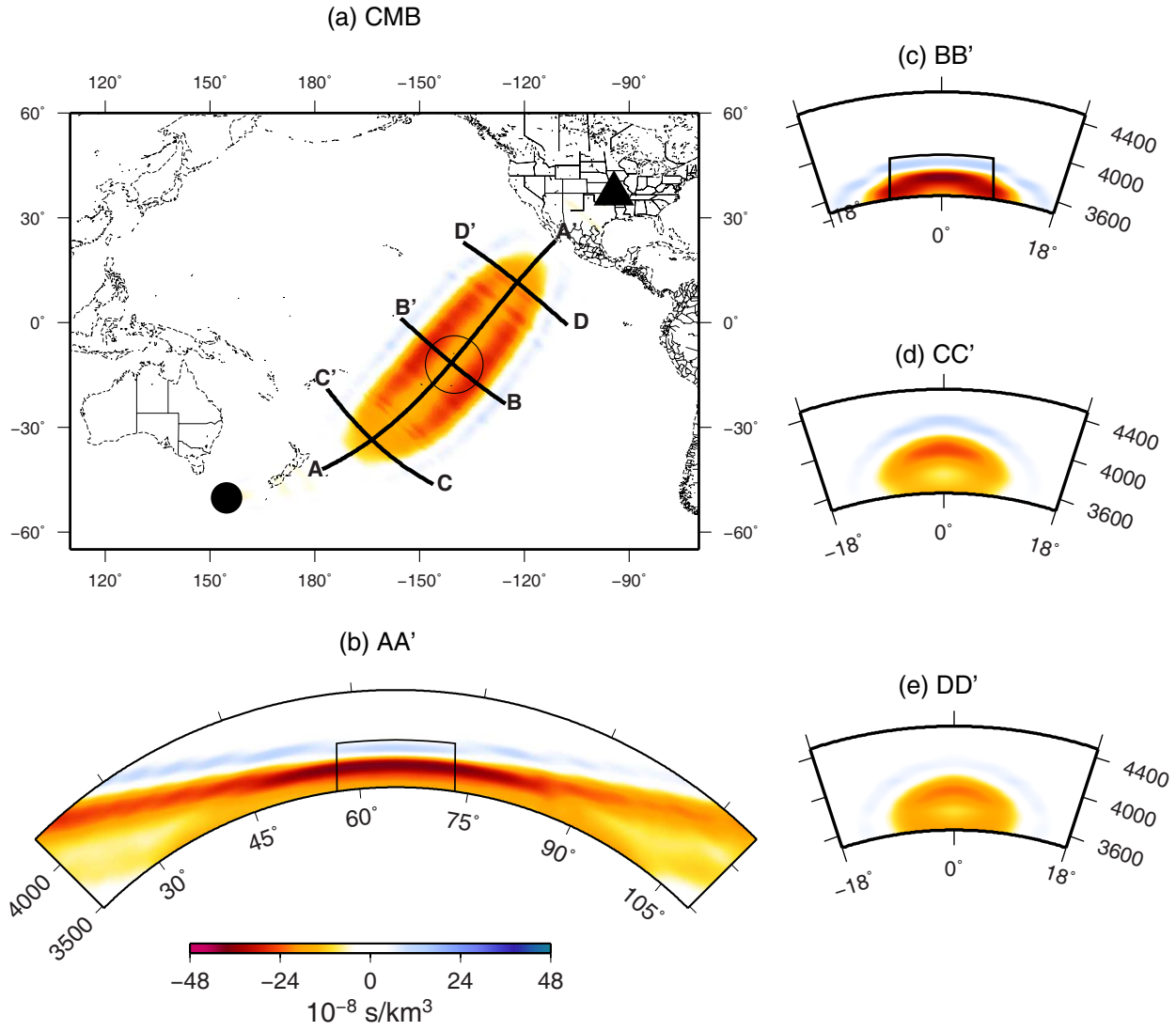

Figure 4.1: *Pdiff* traveltime sensitivity kernel calculated for a cosine taper measurement at the period of 20s. The source-receiver epicentral distance is 130°. Station number is No. 25 in Fig. 3.1. (a) map view of the sensitivity kernel at CMB. (b) -(e) are cross-sections AA′, BB′, CC′ and DD′ showing the sensitivity in the lowermost 1000 km of the mantle. The circle in (a) and black lines in (b) and (c) show the location of the plume anomaly. The source is on the surface and is an explosive source. The radius of the plume anomaly is 500 km.

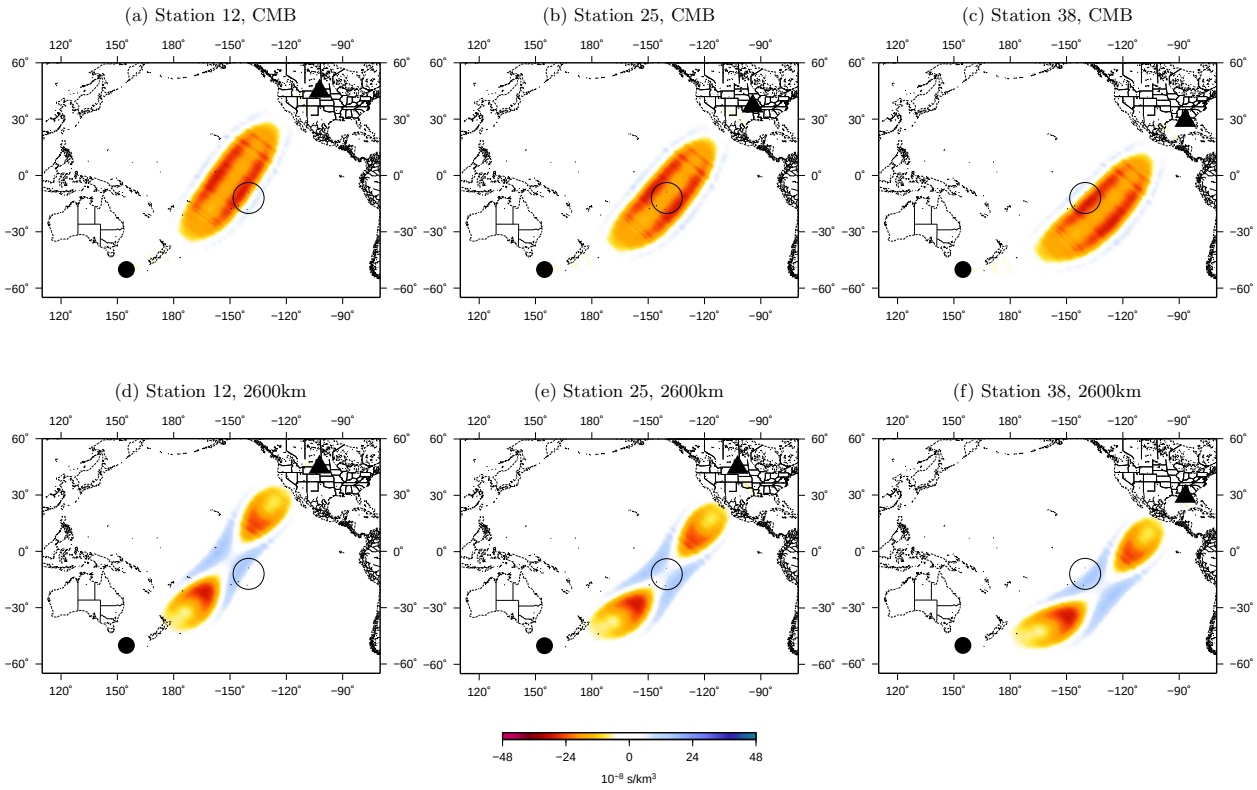

Figure 4.2: *Pdiff* phase delay sensitivity kernel calculated for cosine-taper measurements at a period of 20s at stations 12, 25 and 38. Top figures are sensitivity kernels at the CMB, and bottom figures are sensitivity kernels at 2600 km depth. The circle indicates the location of the plume anomaly with radius of 500 km

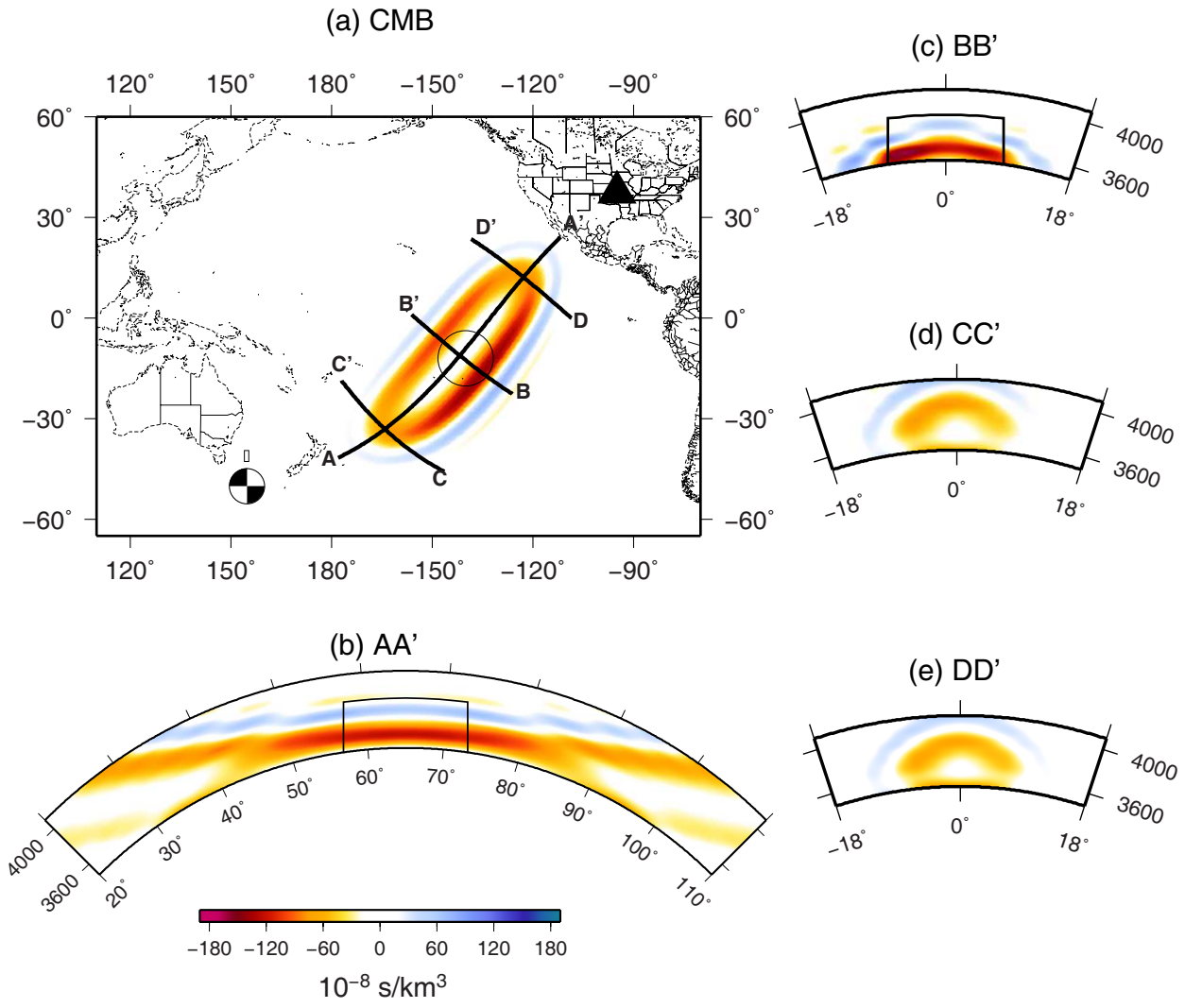

Figure 4.3: The same as Fig. 4.1 but for a *Sdiff* wave. Source mechanism is indicated by the beach ball at the source.

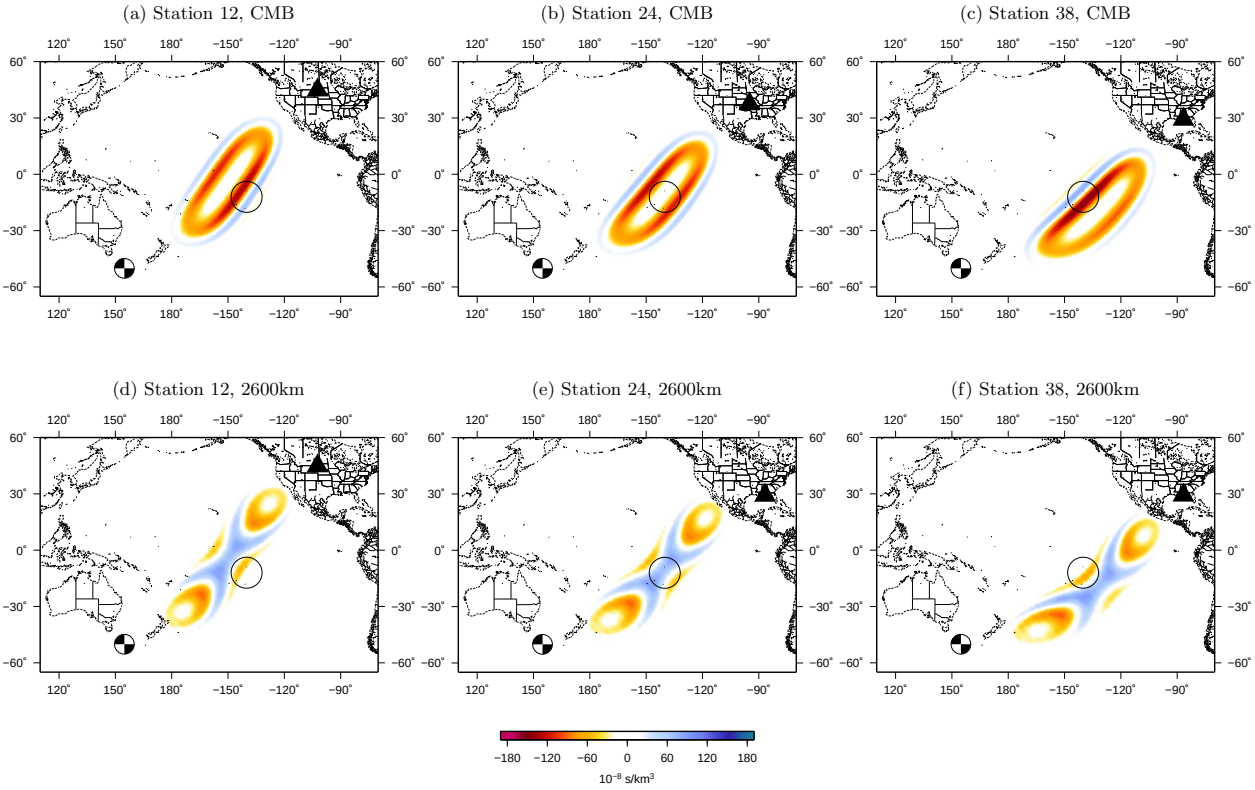

Figure 4.4: The same as Fig. 4.2 but for a *Sdiff* wave.

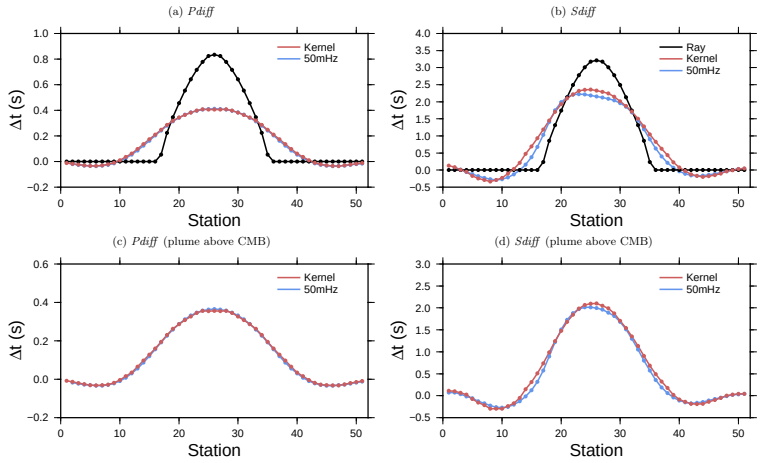

Figure 4.5: Comparison between measurements, ray predictions and finite-frequency kernel predictions for *P*-wave and *S*-wave delay times at the 51 stations. Measured time delays in (c) and (d) are caused by the plume anomaly without wavespeed perturbations in the mesh element (37.5 km) just above the CMB. Horizontal axis is the station number as shown in Fig. 3.1.

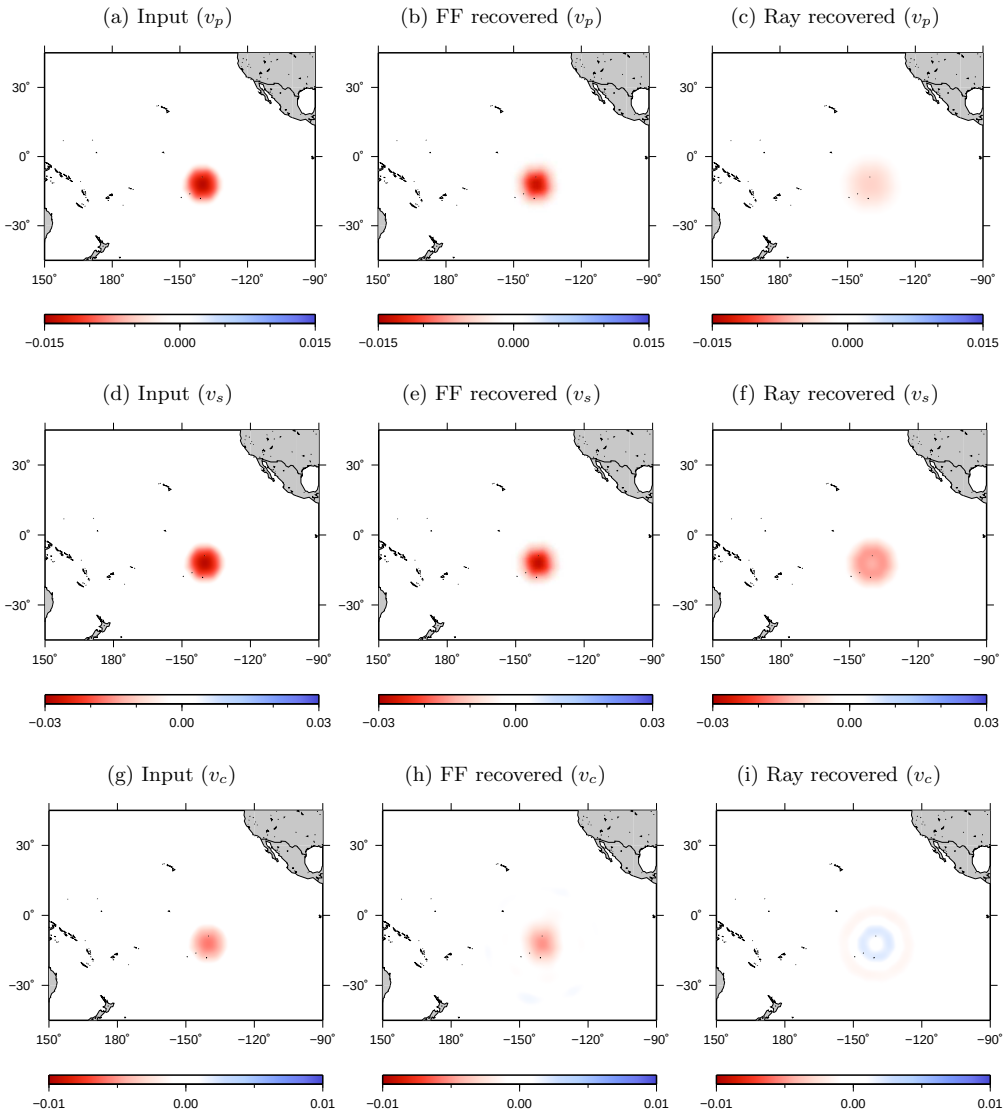

Figure 4.6: Comparison between ray theoretical tomography and finite-frequency tomography. The optimal models are chosen at $\chi^2/N \simeq 1$. The plume anomaly is much better recovered in finite-frequency tomography.

Chapter 5

Conclusion

We simulate global seismic wave propagation in 3-D mantle plume models using Spectral Element Method (SEM) and compare traveltime measurements made on SEM seismograms to predictions based on ray theory. The calculations show strong wave diffraction effects in *P*-wave and *S*-wave traveltimes at periods between 10 to 20 seconds. While wavefront healing effects depend on epicentral distance and plume geometry, *P* waves in general experience strong "healing" effects, which results in an apparent "anti-correlation" between bulk sound speed and S-wave speed anomalies if delay times are interpreted using ray theory.

P-wave and *S*-wave models inverted using ray theoretical tomography at periods between 12 s and 20 s do not resolve the size and anomaly amplitude of input models due to unaccounted wave diffractional effects. For *P* waves and *S* waves of the same period, the size and amplitude of the plume is better constrained in *S* waves. Because of different wave diffractional effects in *P*

waves and *S* waves, bulk sound speed perturbations calculated from ray-theoretical *P*- and *S*- wave models show a polarity change from the input model, regardless of the size of the plume. Ray-theoretical tomographic models inverted using P waves and S waves at same wavelength (different periods) do not recover the input bulk sound speed structure. This confirms intrinsically different scattering between P waves and S waves.

We calculate finite-frequency sensitivity kernels for core-mantle boundary diffracted wave (*Pdiff*) and *Sdiff* to account for wave diffraction effects in imaging deep mantle plumes. Calculations based on finite-frequency sensitivities fit measured traveltimes much better than ray-theoretical predictions. The input plume structure is well recovered in finite-frequency tomography.

It is worth emphasizing that both ray-theoretical analysis and finite-frequency analysis in this paper are based on first-order approximations in a spherically symmetric reference model. The fact that calculations based on finite-frequency sensitivities fit measured traveltimes very well confirms that the relation between traveltime measurements and wavespeed perturbations is close to linear for seismic anomalies in the lowermost mantle (3% in S-wave and 1.5% in P-wave speeds). This is consistent with the study of Mercerat & Nolet (2013) in which they found the relation between cross-correlation delay times and velocity anomalies is close to liner for perturbations up to 10%.

While finite-frequency sensitivity of core-mantle diffracted waves opens the opportunity for high resolution imaging of deep mantle plumes, we point out that we have used perfect path coverage in our tomographic experiments, resolutions of tomographic models in practice are also limited by distributions of earthquakes and stations as well as data quality.

Bibliography

Cobden, L., Mosca, I., Trampert, J., & Ritsema, J., 2012. On the likelihood of post-perovskite near the core-mantle boundary: A statistical interpretation of seismic observations, *Physics of the Earth and Planetary Interiors*, **210**, 21–35.

Dahlen, F. A. & Tromp, J., 1998. *Theoretical Global Seismology*, Princeton University Press.

Dahlen, F. A., Hung, S.-H., & Nolet, G., 2000. Fréchet kernels for finite-frequency traveltimes–i. theory, *Geophysical Journal International*, **141**(1), 157–174.

Davies, D. R., Goes, S., Davies, J. H., Schuberth, B. S. A., Bunge, H. P., & Ritsema, J., 2012. Reconciling dynamic and seismic models of earth's lower mantle: The dominant role of thermal heterogeneity, *Earth and Planetary Science Letters*, **353**, 253–269.

Deschamps, F. & Trampert, J., 2003. Mantle tomography and its relation to temperature and composition, *Physics of the Earth and Planetary Interiors*, **140**, 277–291.

Houser, C., Masters, G., Shearer, P., & Laske, G., 2008. Shear and compressional velocity models

of the mantle from cluster analysis of long-period waveforms, *Geophysical Journal International*, **174**(1), 195–212.

Hung, S. H., Dahlen, F. A., & Nolet, G., 2001. Wavefront healing: a banana-doughnut perspective, *Geophysical Journal International*, **146**(2), 289–312.

Hwang, Y. K., Ritsema, J., van Keken, P. E., Goes, S., & Styles, E., 2011. Wavefront healing renders deep plumes seismically invisible, *Geophysical Journal International*, **187**(1), 273–277.

Ishii, M. & Tromp, J., 2004. Constraining large-scale mantle heterogeneity using mantle and inner-core sensitive normal modes, *Physics of the Earth and Planetary Interiors*, **146**(1-2), 113–124.

Kárason, H. & van der Hilst, R. D., 2001. Tomographic imaging of the lowermost mantle with differential times of refracted and diffracted core phases (pkp, p-diff), *Journal of Geophysical Research-Solid Earth*, **106**(B4), 6569–6587.

Karato, S. & Karki, B. B., 2001. Origin of lateral variation of seismic wave velocities and density in the deep mantle, *Journal of Geophysical Research-Solid Earth*, **106**(B10), 21771–21783.

Kennett, B. L. N. & Fichtner, A., 2012. A unified concept for comparison of seismograms using transfer functions, *Geophysical Journal International*, **191**(3), 1403–1416.

Komatitsch, D. & Tromp, J., 1999. Introduction to the spectral element method for three-dimensional seismic wave propagation, *Geophysical Journal International*, **139**(3), 806–822.

Komatitsch, D. & Tromp, J., 2002. Spectral-element simulations of global seismic wave propagation - i. validation, *Geophysical Journal International*, **149**(2), 390–412.

Laske, G. & Masters, G., 1996. Constraints on global phase velocity maps from long-period polarization data, *Journal of Geophysical Research-Solid Earth*, **101**(B7), 16059–16076.

Lay, T., 2007. *1.18 - Deep Earth Structure Lower Mantle and D*, pp. 619–654, Elsevier, Amsterdam.

Malcolm, A. E. & Trampert, J., 2011. Tomographic errors from wave front healing: more than just a fast bias, *Geophysical Journal International*, **185**(1), 385–402.

Manners, U. J., 2008. Investigating the structure of the core-mantle boundary region using s and p diffracted waves.

Masters, G., Laske, G., Bolton, H., & Dziewonski, A., 2000. *The Relative Behavior of Shear Velocity, Bulk Sound Speed, and Compressional Velocity in the Mantle: Implications for Chemical and Thermal Structure*, pp. 63–87, American Geophysical Union.

Mercerat, E. D. & Nolet, G., 2013. On the linearity of cross-correlation delay times in finite-frequency tomography, *Geophysical Journal Internation*, **192**, 681–687.

Montelli, R., Nolet, G., Dahlen, F. A., & Masters, G., 2006. A catalogue of deep mantle plumes: New results from finite-frequency tomography, *Geochemistry Geophysics Geosystems*, **7**.

Nolet, G. & Dahlen, F. A., 2000. Wave front healing and the evolution of seismic delay times, *Journal of Geophysical Research-Solid Earth*, **105**(B8), 19043–19054.

Nolet, G., Karato, S.-I., & Montelli, R., 2006. Plume fluxes from seismic tomography, *Earth and Planetary Science Letters*, **248**, 685–699.

Ritsema, J. & van Heijst, H. J., 2002. Constraints on the correlation of p- and s-wave velocity heterogeneity in the mantle from p, pp, ppp and pkpab traveltimes, *Geophysical Journal International*, **149**(2), 482–489.

Robertson, G. S. & Woodhouse, J. H., 1995. Evidence for proportionality of p and s heterogeneity in the lower mantle, *Geophysical Journal International*, **123**(1), 85–116.

Schuberth, B. S. A., Zaroli, C., & Nolet, G., 2012. Synthetic seismograms for a synthetic earth: long-period p- and s-wave traveltime variations can be explained by temperature alone, *Geophysical Journal International*, **188**(3), 1393–1412.

Su, W. J. & Dziewonski, A. M., 1997. Simultaneous inversion for 3-d variations in shear and bulk velocity in the mantle, *Physics of the Earth and Planetary Interiors*, **100**(1-4), 135–156.

Tan, E. & Gurnis, M., 2005. Metastable superplumes and mantle compressibility, *Geophysicsl Research Letters*, **32**.

Thomson, D. J., 1982. Spectrum estimation and harmonic-analysis, *Proceedings of the Ieee*, **70**(9), 1055–1096.

Thorne, M. S. & Garnero, E. J., 2004. Inferences on ultralow-velocity zone structure from a global analysis of $spdks$ waves, *Journal of Geophysical Research-Solid Earth*, **109**(B08301).

Trampert, J., Vacher, P., & Vlaar, N., 2001. Sensitivities of seismic velocities to temperature, pressure and composition in the lower mantle, *Physics of the Earth and Planetary Interiors*, **124**(3-4), 255–267.

Trampert, J., Deschamps, F., Resovsky, J., & Yuen, D., 2004. Probabilistic tomography maps chemical heterogeneities throughout the lower mantle, *Science*, **306**(5697), 853–856.

Tromp, J., Tape, C., & Liu, Q., 2005. Seismic tomography, adjoint methods, time reversal, and banana-donut kernels, *Geophysical Journal International*, **160**, 195–216.

Zhou, Y., 2009. Multimode surface wave sensitivity kernels in radially anisotropic earth media, *Geophysical Journal International*, **176**(3), 865–888.

Zhou, Y., Dahlen, F. A., & Nolet, G., 2004. Three-dimensional sensitivity kernels for surface wave observables, *Geophysical Journal International*, **158**(1), 142–168.

Zhou, Y., Nolet, G., Dahlen, F. A., & Laske, G., 2006. Global upper-mantle structure from finite-frequency surface-wave tomography, *Journal of Geophysical Research-Solid Earth*, **111**(B4).